Estimating the Global Oil-Gas Methane Emission Rate Distribution at Facility Scale using Multiple Satellite Systems

Dylan Jervis¹ (dylan.jervis@ghgsat.com), Jean-Philippe W MacLean¹, Jason McKeever¹, Mathias Strupler¹, Antoine Ramier¹

¹GHGSat Inc, Montreal, QC, Canada

KEYWORDS: Methane, oil and gas, remote sensing, detection probability, coverage, point source

SYNOPSIS: The methane emission rate distribution of facility-scale oil and gas sources is estimated using multiple high-resolution satellite systems.

ABSTRACT:

We estimate the global oil and gas (O&G) emission rate distribution above ~20 kg h⁻¹ at facility scale using 16,294 quantified O&G methane emission rates detected from five high-resolution satellite instrument/data processing combinations in 2024 and 2025 (GHGSat/GHGSat, Tanager/Carbon Mapper, EMIT/Carbon Mapper, Sentinel-2/IMEO-MARS, Landsat/IMEO-MARS). We find that the emission rate distribution is well-described by a lognormal model. Because our estimation method explicitly incorporates a model for each system's detection sensitivity, we simultaneously retrieve the facility scale, conditionaveraged "survey-mode" detection probability for each satellite system. We estimate the relative spatiotemporal coverage of each satellite system directly from their measured emission rates and quantify the effective spatial coverage by calculating the Earth Mover's Distance between each satellite system's plume detection locations and the Global Fuel Exploitation Inventory v3 O&G predictions, estimating that all satellite systems have global coverage of O&G emissions within sampling error. The O&G facility scale emission rate distribution estimate is constrained by the largest collection of satellite detections to date, providing valuable information about the expected number of O&G emission events at different emission rates. Finally, the detection probability, spatial and temporal coverage estimates are combined into a total relative observation completeness metric for each satellite system that should be of interest to research and policy makers for understanding the relative survey capabilities of different high-resolution satellite systems.

INTRODUCTION

Methane is second only to CO₂ in its contribution to global warming¹. Anthropogenic methane sources are responsible for the majority of methane emissions and, consequently, reducing emissions from anthropogenic sources has received significant attention in recent years owing to methane's relatively short atmospheric lifetime and potential to be mitigated at low-cost. The oil and gas (O&G) sector is responsible for over 20% of total anthropogenic methane emissions². However, methane emissions from O&G sources are hard to accurately model and predict due to a combination of factors, including that emission events can have instantaneous emission rates that vary by orders of magnitude^{3–10}. The emission rate distribution quantifies the fraction of events detected at different emission rates and is therefore a key metric for characterizing O&G sector methane emissions: it can help refine bottom-up inventory estimates^{11–14}; can reveal the portion of large, "super-emitting" sources for which there exists efficient mitigation opportunities^{4,6,15,16}; and can help inform detection technology requirements¹⁷. Satellite remote sensing instruments offer detection capability at global scale, frequent temporal revisits (hourly-to-weekly) over extended time periods (>5 years per mission), allowing for a comprehensive measurement of the global O&G emission distribution.

Over the past decade, a new generation of space-based methane imaging spectrometers have been shown to be capable of detecting methane emissions at facility scale spatial resolution. Sentinel-2 and Landsat-9 provide methane information with 20 and 30 m ground sample distance (GSD)^{4,18}, respectively, but with relatively poor sensitivity (>20% of background^{19,20}) at 5 – 16 day revisit periods; the Earth Surface Mineral Dust Source Investigation (EMIT) instrument provides methane column density enhancements²¹ at 60 m GSD with moderate precision (~5% of background²⁰); while the GHGSat constellation^{22,23} and the Tanager-1 satellite from Carbon Mapper²⁴ provide targeted monitoring at ~30m resolution and good column density precision (~1-2% of background). Together these instruments comprise a global methane observing system that enables detection and attribution of methane emissions at the facility scale. Other high-resolution instruments in orbit (e.g. PRISMA, EnMAP, WorldView-3) can detect methane plumes yet currently yield fewer detections than the systems noted above.

A measured emission-rate distribution reflects the spatial resolution, sensitivity and spatiotemporal coverage of the measurement system that produced it. A system with fine spatial resolution is able to resolve distinct sources that would be aggregated into a single emission for instruments with coarser spatial resolution^{7,14,25}. A system that reliably detects only larger emissions reveals little about the true distribution at smaller emission rates. Conversely, an instrument with near-perfect sensitivity but limited geographic or temporal coverage provides an incomplete view of emissions

occurring outside its sampling window. Any empirical estimate of an emission rate distribution must therefore account for the differing spatial resolution, detection thresholds and spatio-temporal coverage of the measurement systems contributing to the dataset.

MATERIALS AND METHODS

Materials

The O&G methane emission catalogues used in this study are produced not by the satellites alone, but by the organizations that convert raw imagery and/or methane column density measurements into plume detections and emission-rate estimates. Because the plume detection and emission rate quantification methods strongly influence how many plumes are found and how accurately they are quantified, we treat each satellite instrument + data processing and provider pair as a single system when evaluating detection performance and spatiotemporal coverage. The specific data processing organizations considered in this study are GHGSat, Carbon Mapper, and the Methane Alert and Response System service of the UN Environment Program's International Methane Emissions Observatory (IMEO-MARS). For some instruments, the organization that designs and operates and operates the instrument is the same as the data processing organization that distributes it (e.g. GHGSat and Tanager/Carbon Mapper). Other instruments (EMIT, Sentinel-2, and Landsat) have their data processed by multiple data provider organizations. For EMIT, like Tanager, we use the Carbon Mapper data catalogue (https://data.carbonmapper.org/) owing to the close relationship between Carbon Mapper and NASA-JPL who operate EMIT. For Sentinel-2 and Landsat, we rely on the IMEO-MARS database (https://methanedata.unep.org/). By analyzing these combined instrument/processing systems, we capture the real-world performance that users encounter when they rely on each data source.

Methods

Let $Q_k = \{Q_1, Q_2, ..., Q_{N_k}\}$ be the emission rates of plumes detected by satellite system k. The probability density distribution of a detected emission Q_i is

$$f(Q_i|\mathbf{z}_k,\boldsymbol{\theta}_k) = \frac{POD(Q_i;\mathbf{z}_k)\rho(Q_i;\boldsymbol{\theta}_k)}{Z_k(\mathbf{z}_k,\boldsymbol{\theta}_k)}$$
(1)

and, correspondingly, the likelihood of satellite system k detecting the emission rates Q_k is given by the product of these terms

$$\mathcal{L}(\mathbf{z}_k, \boldsymbol{\theta}_k | \boldsymbol{Q}_k) = \prod_{i=1}^{N_k} f(Q_i | \mathbf{z}_k, \boldsymbol{\theta}_k).$$
 (2)

We assume that all detected emission rates are independent of each other. Here, the probability of detection is modelled as a lognormal cumulative distribution function

$$POD(Q; \mathbf{z}_k) = 1 - \frac{1}{2} \operatorname{Erfc}\left(\frac{\ln(Q) - \ln(Q_{k;det})}{\sqrt{2}s_k}\right)$$
(3)

with the parameter vector $\mathbf{z}_k = \{Q_{k;det}, s_k\}$. The emission rate density distribution is modelled as a lognormal probability distribution function

$$\rho(Q; \boldsymbol{\theta}_k) = \frac{1}{O\sigma_k \sqrt{2\pi}} e^{-\frac{(\ln(Q) - \mu_k)^2}{2\sigma_k^2}}$$
(4)

with the parameter vector $\boldsymbol{\theta}_k = \{\mu_k, \sigma_k\}$, and the normalization constant is given by

$$Z_k(\mathbf{z}_k, \boldsymbol{\theta}_k) = \int_0^\infty POD(Q; \mathbf{z}_k) \rho(Q; \boldsymbol{\theta}_k) dQ.$$
 (5)

We fit parameters by minimizing the negative log likelihood

$$-\log \mathcal{L}(\mathbf{z}_k, \boldsymbol{\theta}_k | \boldsymbol{Q}_k) = -\sum_{i=1}^{N_k} [\log \rho(Q_i; \boldsymbol{\theta}_k) + \log POD(Q_i; \mathbf{z}_k)] + N_k \log Z_k(\mathbf{z}_k, \boldsymbol{\theta}_k).$$
 (6)

We estimate the probability of detection and emission rate distribution functions in a two-stage process. First, we assume a common emission rate distribution across all satellite systems, i.e. $\boldsymbol{\theta}_{com} = \boldsymbol{\theta}_k$ for all k, and minimize the summed negative log likelihood over all satellites to obtain the parameters $\{\hat{\boldsymbol{z}}_{joint;k}, \hat{\boldsymbol{\theta}}_{joint}\}$. We estimate errors on the retrieved parameters using a non-parametric bootstrap method where B = 500 samples of data of length N_k are sampled, with replacement, for each satellite system. We refit each data sample, yielding estimates $\{\hat{\boldsymbol{z}}^{(b)}_{joint;k}, \hat{\boldsymbol{\theta}}^{(b)}_{joint}\}_{b=1}^{B}$. The standard errors $\delta\hat{\boldsymbol{z}}_{joint;k}$ and $\delta\log\hat{\boldsymbol{\theta}}_{joint;k}$ are computed from these bootstrap estimates.

Second, for each satellite system k, we re-estimate both the probability of detection and emission distribution parameters for each satellite system independently, with Bayesian constraints provided by the joint estimates, by minimizing

$$f_k(\mathbf{z}_k, \boldsymbol{\theta}_k) = -\log \mathcal{L}(\mathbf{z}_k, \boldsymbol{\theta}_k | \boldsymbol{Q}_k) + \sum_j \frac{\left(z_{k;j} - \hat{z}_{joint;k;j}\right)^2}{\delta \hat{z}^2_{joint;k;j}} + \sum_j \frac{\left(\log \theta_k - \log \hat{\theta}_{joint;k;j}\right)^2}{(\delta \log \hat{\theta}_{joint;k;j})^2}$$
(7)

which is equivalent to a maximum a posteriori estimate with independent Gaussian priors centered at the joint fit parameter results with variances given by the bootstrap standard errors. This yields per-satellite system estimates $\{\hat{\boldsymbol{z}}_k, \hat{\boldsymbol{\theta}}_k\}$. From these parameter estimates, we can estimate the probability of detection for each satellite system $POD_k(Q; \hat{\boldsymbol{z}}_k)$ as well as the pooled emission rate distribution $\rho(Q; \langle \hat{\boldsymbol{\theta}} \rangle)$ were $\langle \hat{\boldsymbol{\theta}} \rangle = \frac{1}{K} \sum_{k=1}^{K} \hat{\boldsymbol{\theta}}_k$ is the average of the emission rate distribution parameters estimated across all satellite systems.

To justify our two-stage estimation method, we compare joint and per-satellite fits. As documented in the supporting information, per-satellite retrieved emission rate distributions yield a lower

summed Akaike Information Criteria (AIC) than a single common emission rate distribution, indicating genuine instrument-specific differences. However, the empirical-Bayes penalty centered on the joint solution stabilizes weakly identified parameters and prevents overfitting. All further results in this paper that require a single emission rate distribution use the pooled estimate $\rho(Q; \langle \hat{\theta} \rangle)$, while the detection probabilities $POD_k(Q; \hat{\mathbf{z}}_k)$ are reported per satellite system with bootstrap uncertainties.

For illustration purposes, the measured emission rate probability density distributions are partitioned into m=25 logarithmic bins with edge positions $e_i=10^{-3+0.2i}$ t hr⁻¹ (i=0,...,m+1) and widths $w_i=e_{i+1}-e_i$ (i=0,...,m). These edge positions encompass the minimum (0.018 t h⁻¹) and maximum emission rates (225 t h⁻¹) present in this study. For satellite system k, let $n_{k,i}$ be the number of detected plumes in bin window i and $N_k=\sum_{i=1}n_{k,i}$ be the total. The empirical bin probability densities are $p_{k,i}=n_{k,i}/(N_kw_i)$ with normalization such that $\sum_{i=1}p_{k,i}w_i=1$. To compare to the data, we plot the binned estimated probability density model $\hat{p}_{k,i}(\hat{z}_k, \hat{\theta}_k)$

$$\hat{p}_{k,i}(\hat{\mathbf{z}}_k, \hat{\boldsymbol{\theta}}_k) = \frac{\int_{e_i}^{e_{i+1}} POD(Q; \hat{\mathbf{z}}_k) \rho(Q; \hat{\boldsymbol{\theta}}_k) dQ}{Z_k(\hat{\mathbf{z}}_k, \hat{\boldsymbol{\theta}}_k) w_i}.$$
 (8)

RESULTS AND DISCUSSION

A map showing the detected locations of all O&G facility scale methane emissions detected in 2024 by the satellite systems considered in this study, and part of 2025 for the case of Tanager/Carbon Mapper, are shown in Figure 1. Of these 16,294 quantified emissions, 11,752 are from GHGSat/GHGSat, 2,284 are from Tanager/Carbon Mapper, 460 are from EMIT/Carbon Mapper, 732 are from Landsat/IMEO-MARS, and 1,066 are from Sentinel-2/IMEO-MARS. Emissions are distributed globally, with notable clusters of emissions in North America, North Africa, and Central Asia. In Figure 2a, we show the relationship between the cumulative number of unique 0.5° x 0.5° grid cells where satellite system k detected an emission and the cumulative number of detected plumes. The grey 1:1 line represents the regime in which each detection occurs in a unique location. Departures from this line indicate locations where multiple plumes were seen over the study time period and we note the similar shapes of these excursion curve across the different satellite systems suggesting similar underlying source heterogeneity. We can see that GHGSat/GHGSat detected plumes in the largest number of unique detection locations M_k , as well as detecting the largest number of plumes N_k . Landsat/IMEO-MARS and Sentinel-2/IMEO-MARS – even though they detect more plumes than EMIT/Carbon Mapper – do so over fewer locations. In Figure 2b, we attempt to quantify how representative the spatial distribution of detected O&G emission events from each satellite system are to the best estimate of the expected spatial distribution by calculating the Earth Mover's Distance (EMD) between the collection of M_k 0.5° x 0.5°

unique detection locations (unweighted by detection counts) and the O&G emissions estimated by the Global Fuel Exploitation Inventory version 3 (GFEIv3)²⁶. The EMD estimates the minimum amount of work required to transform one spatial distribution into another and is described in the supplementary information. For reference, we calculate i) the EMD for grid cells in the Permian basin region where any of the satellite systems made a detection and the full, global GFEIv3, and ii) the EMD between M_k random, emission-weighted, samples of GFEIv3 and the full GFEIv3 emissions prediction. For i), we observe that all satellite systems have EMDs much lower than the Permian-GFEIv3 EMD, quantifying the spatial coverage advantage that global satellite systems possess in comparison to Permian aircraft survey campaigns, for example those described in Ref^{6,7,15,16}. For ii), we show that all satellite system EMDs are within the (10%, 90%) random sampling EMD values of GFEIv3, suggesting that all satellite systems considered here have representative global coverage of the expected spatial distribution of global O&G emissions. The GHGSat/GHGSat EMD is the lowest of all the satellite systems, indicating that the locations where it detected plumes were most spatially similar to the GFEIv3 O&G emissions. The EMD of Sentinel-2/IMEO-MARS is approximately 3.5x larger than that of GHGSat/GHGSat, indicating that the locations of its detected emissions were approximately 3.5x farther away to GFEIv3 per unit of emission. The EMD values from M_k samples of GFEIv3 indicate that the EMD is sample-number dependent (at least for this situation where there are many more non-zero GFEIv3 grid cells than grid cells with plume detections): the satellite systems with the largest number of unique detection locations M_k have the smallest EMDs with respect to GFEIv3.

The measured emission rate density distributions p_k for each instrument/data provider system k are shown in Figure 3 alongside the modelled bin probability densities $\hat{p}_k(\hat{z}_k, \hat{\theta}_k)$. Colloquially, the emission rate corresponding to the peak of the distribution has been understood to be indicative of the detection limit. We note that these peak positions are separated by roughly an order of magnitude, from ~200 kg h⁻¹ (GHGSat/GHGSat and Tanager/Carbon Mapper) to ~2 t hr⁻¹ (Landsat/IMEO-MARS). We retrieve the following parameters for the lognormal parent distribution $\langle \hat{\theta} \rangle = (\hat{\mu}, \hat{\sigma}) = (-6.72^{+0.70}_{-0.72}, 2.56^{+0.22}_{-0.19})$ where the errors correspond to the minimum and maximum across the per satellite system estimates and the parameters are for emission rates Q expressed in units of t h⁻¹. We plot the retrieved emission distribution model $\rho(Q; \langle \hat{\theta} \rangle)$ in Figure 4a. A lognormal form of the emission rate distribution has been found to best describe the facility scale (150 m) emission rate distributions measured with airborne instruments over the Permian basin⁷ for emission rates between 3 – 1,000 kg h⁻¹. We note that our retrieved distribution resembles a power-law $p \propto Q^{-\alpha}$ with an exponent of approximately α = 2.3 (see supporting information), roughly consistent with what has been previously observed for both airborne and satellite data^{5,25,27}. We present analysis in the supplementary information showing that the

lognormal fit model yields a lower AIC than a power-law model for the common emission-rate distribution assumption, implying that the lognormal model describes—and predicts—the measurements more effectively. We note that our estimated lognormal distribution for O&G facility scale emissions is only informed between the minimum and maximum emission rates for which we have empirical data – i.e. between the ~0.02 t hr⁻¹ and 225 t hr⁻¹ emission events detected by GHGSat/GHGSat. Therefore, the global O&G facility scale emission rate distribution remains unconstrained in our study outside of these emission rates. In principle, this makes it impossible to infer a cumulative distribution function $CDF_{parent}(Q) = \int_0^Q \rho(Q')dQ$ since the CDF presumes knowledge of the emission rate distribution for arbitrarily low emission rates. Finally, the facility scale O&G emission rate distribution estimated here should be understood as distinct from an emission rate distribution measured at the spatial resolution of individual equipment (< 10 m). Airborne measurements at 2 m GSD of in the Permian⁷ have shown that emission rate distributions at the equipment scale (2 m GSD) and facility scale (2 m GSD measurements aggregated to 150 m) have different shapes, especially at emission rates that within the partial detection region. Numerical experiments have also shown the emission rate distribution to be dependent on spatial resolution²⁵. In the supplementary information (S6), we develop simulations, an analytical model, and perform cross-sensor comparisons in the Permian basin (2 m airborne, ~30 m satellite, and ~7 km satellite), to show that the tail of the measured emission rate distribution is likely resolution-invariant.

Our estimate of the O&G facility scale emission rate distribution is distinguished from previous remote sensing estimates^{4–7,15,16,28} in a two significant ways. First, the analysis uses an unprecedented global sample of individual plumes—an order of magnitude more than previous studies^{4,5} – and uses new satellite systems with much more sensitive detection performance. This reveals O&G facility scale emission rate behaviour across a wider range of emission rates, and with greater statistical confidence. Second, we incorporate each instrument's detection probability directly in the O&G emission rate distribution analysis. By fitting the measured emission rate distributions to a function comprised of the emission rate distribution and detection probabilities simultaneously, we are able distinguish which portions of the measured distribution are affected by sensor sensitivity, and by how much.

We note that several methods have been proposed, and used, to quantify detection probability. Controlled release measurement campaigns^{22,29–31} are the most widely regarded method for establishing benchmark detection probability and quantification accuracy performance. Controlled release experiments typically comprise a relatively small number observations (typically between 5 and 100) in which methane is released from a specified location and the truth rate is measured with high accuracy on the ground. A second estimate is then made using the satellite measurement and compared to the ground truth

rate. The main limitations of controlled release experiments are that 1) the small number of observations available limit the ability to perform a proper statistical inference of the detection limit and quantification accuracy, especially to different environmental and observation conditions encountered in nominal operations and 2) there is generally prior knowledge about both the release location as well as the special nature, or importance of, controlled release observations. Therefore, while the detection limit inferred from controlled release measurements is appropriate for "target-mode" observations of pre-determined sites, it may be less suitable for "survey-mode" observations over the complete range of observational conditions encountered by the satellite system, where both the existence and location of emitting sites in unknown. The latter situation describes the plume catalogue dataset studied here. In addition, controlled releases typically involve a single source, whereas in nominal operations multiple equipment-scale plumes may be aggregated within one facility scale detected emission. Such aggregation can produce a peak in the aggregated emission rate distribution²⁵ that, if at-or-above the partial detection region of the satellite system and not modeled, can lead to an estimated detection probability that is biased to larger rates (i.e. larger Q_{k-det} . See section S6 for further explanation).

The retrieved survey-mode detection probability model parameters for each satellite are tabulated in Table S2 and the estimated detection probability models are shown in Figure 4b. We highlight that this detection probability estimate averages over the ensemble of environmental and viewing conditions encountered. When comparing to controlled release results for GHGSat^{22,32} we find that an inferred survey-mode value at 50% probability of detection of $\hat{Q}_{GHGSat:det}$ =0.46 t h⁻¹ that is approximately 4.5x higher than the controlled release "target-mode" value of 0.1 t hr⁻¹ (at 3 m s⁻¹ wind speed). Compared to a similar experiment for EMIT performed with nearly coincident aircraft measurements used as a proxy for ground truth, the survey-mode value $\hat{Q}_{EMIT:det}$ =1.87 t h⁻¹ is approximately 2.5x higher than the ~0.7 t h⁻¹ (at 3 m s⁻¹ wind speed) reported value³³. This discrepancy extends to airborne sensors as well: AVIRIS has and estimated 50% detection probability below 10 kg hr⁻¹ in controlled release tests³⁴, but qualitative inspection of field campaign cumulative emission rate distributions 16,35 has estimated the detection limit to be above ~100 kg h⁻¹; Bridger GML controlled release testing has demonstrated a 50% detection probability of ~0.3 kg h⁻¹ per m s⁻¹ of wind speed³⁶, but a measured source-resolved emission rate distribution from a Permian campaign (average wind speed of 4.9 m s⁻¹, giving a 50% controlled release detection probability estimate of ~1.5 kg h⁻¹) shows a distribution peak⁷ occurring above 3 kg h⁻¹ which, based on the consistent trend in our satellite system analysis, would imply a 50% POD emission rate in excess of 3 kg h⁻¹. We expect similar differences between controlled release and survey-mode detection probabilities to persist for other satellite systems if/when controlled release results for each become available. Beyond the possible spatial aggregation effect mentioned above, we hypothesize that these

differences are due to differences in both the prior knowledge available in controlled release experiments, and the range – or lack thereof - of observational and environmental conditions (e.g. different albedos, wind speeds, observation geometries, solar zenith angles, etc.). An empirical study of GHGSat methane retrievals found that albedo was a strong driver of column density precision²², and both a controlled release³² and situational study³⁷ have established the dependence of detection probability on wind speed. Therefore, we suggest that the width $\hat{s}_k^2 = s_{k;0}^2 + \text{Var}[\ln(\delta\Omega) + \ln(u)]$ of the survey-mode detection probability function is due to the increased variance due to averaging over different precision and wind conditions over the situation-specific statistical width $s_{k;0}$ encountered in controlled release experiments. Finally, we note the sensitivity of the estimated detection probability on the estimated emission rate distribution, evident in Equation 1.

The estimated survey-mode detection probabilities $POD(Q; \hat{\mathbf{z}}_k)$ can be used alongside the estimated distribution $\rho(Q; \langle \hat{\boldsymbol{\theta}} \rangle)$ to compare satellite systems under the conditions of equal spatio-temporal coverage by their expected detection fraction Z_k introduced in equation 1 of the methods section. We report a relative survey-mode detection completeness c_D , akin to the absolute completeness measure introduced in Ref.²⁰

$$c_{D;k} = \frac{Z_k}{\max_j(Z_j)} \tag{9}$$

We restrict ourselves to a relative detection fraction measure given our ignorance of the global emission rate distribution below ~0.02 t h⁻¹, the smallest emission rates for which we have empirical data. We find GHGSat/GHGSat to be the most sensitive system with $100\%_{-2\%}^{+6.4\%}$ relative detection completeness, with Tanager/Carbon Mapper having similar detection capability, detecting $93\%_{-2\%}^{+12\%}$ of plumes compared to GHGSat/GHGSat for equal spatiotemporal coverage. EMIT/Carbon Mapper, Landsat/IMEO-MARS, and Sentinel-2/IMEO-MARS are estimated to be able to detect $(20.8\%_{-0.4\%}^{+6.0\%}, 8.7\%_{-0.3\%}^{+1.7\%}$ and $10.8\%_{-0.2\%}^{+2.6\%}$) of the plumes as GHGSat/GHGSat for equal spatio-temporal coverage. Figure 4a shows the scaled, or unnormalized, measured and modelled emission rate density distribution, $p_k \cdot Z_k$ and $\hat{p}_k(\hat{z}_k, \hat{\theta}_k) \cdot Z_k$. We can see how the scaled distributions overlap for emission rates above their respective partial detection regions, as they should when $POD \rightarrow 1$, explicitly illustrating how the combined satellite systems can constrain the emission rate distribution estimate.

We propose a method to estimate a sensor's effective spatio-temporal coverage directly from plume counts and Z_k , rather than from retrieval-area coverage or revisit rates (which are, in general, unavailable and/or not always comparable between satellite systems). The expected number of facility

scale detections for satellite system k is $N_k = N_{k;occ}Z_k$ where Z_k is the expected detection fraction over the actual set of observation opportunities used by satellite system k, and $N_{k;occ}$ is the expected number of plume occurrences that happened when, and where, the system observed. Therefore, we can define the relative spatio-temporal coverage, or completeness, as:

$$c_{ST;k} = \frac{N_{k;occ}}{\max_{j} (N_{j;occ})} = \frac{\frac{N_k}{Z_k}}{\max_{j} \left(\frac{N_j}{Z_j}\right)}.$$
 (10)

We find that GHGSat/GHGSat has the largest relative spatio-temporal coverage with $c_{ST} = 100\%_{-6\%}^{+2\%}$. Therefore, all c_{ST} are scaled relative to the GHGSat/GHGSat system and are shown in Figure 5b. We estimate that Landsat/IMEO-MARS and Sentinel-2/IMEO-MARS have roughly similar spatio-temporal coverage with c_{ST} equal to $(72\%_{-11\%}^{+3\%}, 84\%_{-16\%}^{+1\%})$ of GHGSat/GHGSat, respectively. We estimate that Tanager/Carbon Mapper - after scaling the 2,284 O&G plumes it has detected between September 2024 and August 2025 to an estimated 4,025 for a full year's worth of detections at full operational capacity (see supporting information) — would have a relative spatiotemporal completeness of $37\%_{-4\%}^{+1\%}$, and EMIT/Carbon Mapper $19\%_{-4\%}^{+1\%}$. We add that, given that all satellite systems were found to have representative global spatial coverage of O&G emissions through the EMD investigation, it would be reasonable to factor out an equal spatial coverage component of the relative spatio-temporal completeness metric and interpret c_{ST} instead as a relative temporal completeness.

Finally, the survey-mode detection and spatio-temporal completeness measures can be combined as a product to estimate a total relative survey-mode emission event completeness measure shown in Figure 5c. We can see how the total relative emission event completeness reduces, intuitively, to a relative comparison of detected plume totals by each instrument

$$c_k = \frac{N_{k;occ} \cdot Z_k}{\max_j \left(N_{j;occ} \cdot Z_j\right)} = \frac{\frac{N_k}{Z_k} \cdot Z_k}{\max_j \left(\frac{N_j}{Z_j} \cdot Z_j\right)} = \frac{N_k}{\max_j \left(N_j\right)}$$
(11)

while the decomposition of c_k indicates how much comes from coverage versus detectability. Given that GHGSat/GHGSat detected the most plumes, it is defined as having a total relative emission completeness of $100\%_{-8\%}^{+9\%}$; Tanager/Carbon Mapper has $34\%_{-4\%}^{+5\%}$; EMIT/Carbon Mapper has $3.9\%_{-0.9\%}^{+1.2\%}$; Landsat/IMEO-MARS has $6.2\%_{-1.2\%}^{+1.4\%}$; and Sentinel-2/IMEO-MARS has $9.1\%_{-1.9\%}^{+2.3\%}$.

There are differences worth highlighting between the relative completeness measures developed here and the absolute completeness definition introduced in Ref²⁰. Starting with the absolute emission event detection completeness, the original definition implicitly requires knowledge of the true global emission rate distribution for all emission rates Q, including in the $Q \rightarrow 0$ t h⁻¹ limit. Although aircraft campaigns in the Permian^{6.7,14–16,20} and continental USA²⁸ have studied the emission rate distribution with sensitivity down to the kg h⁻¹ level, these studies are still far from constraining the complete global distribution across the entire range of rates. For that reason, we introduced a relative detection completeness measure c_D which only quantifies completeness with respect to the subset of the distribution that is actually observed. The absolute temporal completeness measure likewise presumes prior knowledge of the source persistence P. In reality, the true persistence is unknown and the measured persistence is a function of an instrument's detection probability³⁸, $P(POD(Q; \hat{z}_k))$. Our relative spatiotemporal completeness measure, c_{ST} , relies only on the empirically sampled detection record. The relative completeness framework provides a practical and transparent measure of how well current observing systems constrain methane emissions in the face of still-unknown complete global emission rate and persistence distributions.

We note that many of the satellite systems here either already have, or are projected to, increase their observation capacity since the 2024 study period: GHGSat launched 2 more satellites in June 2025, GHGSat-C12 and C13, and has plans to launch an additional 2 instruments in 2025, plus more in 2026; Carbon Mapper is currently developing the Tanager-2, 3 and 4 satellite instruments; Sentinel-2c was launched in September 2024; and the Sentinel-5 mission was launched in August 2025. These new instruments will increase the spatio-temporal coverage of the satellite systems relative to the 2024 measure c_{ST} estimated here. The detection completeness may also improve for all systems as organizations develop better methods to reduce column density precision and better identify plume enhancements.

We suggest that these results may be useful for those who want to aggregate data from multiple instruments with different sensitivities and coverage. An estimate of the facility-scale, survey-mode detection probability derived under nominal conditions for different instruments can be used to estimate the persistence of a source using the multi-sensor persistence methods introduced in Ref³³ and, alongside the estimate of the relative spatio-temporal coverage of each satellite system, better constrain time-averaged emission rate estimates for improving inventory estimates^{5,20,36}. The estimated O&G facility scale emission rate distribution may be useful to researchers and policy makers for constraining of total plume emissions occurring at certain emission rates.

SUPPORTING INFORMATION

Additional description of the satellite instruments (Text S1), the Akaike Information Criteria for determining best estimation functions (Text S2; Fig. S1), the Earth Movers Distance (Text S3; Fig. S2; Table S1), the estimation of the annual Tanager-1 O&G plume count (Text S4; Fig. S3), joint and satellite system specific POD and PDF estimates (Text S5; Tables S2), and the spatial resolution dependence of measured emission rate distributions (Text S6; Figures S3 and S4).

CORRESPONDING AUTHOR

*Dylan Jervis (dylan.jervis@ghgsat.com)

AUTHOR CONTRIBUTIONS

DJ conceived the study, performed the analysis, and wrote the first draft of the manuscript. All authors contributed to the interpretation of the results and the writing of the manuscript.

ACKNOWLEDGEMENTS

The authors thank Dan Cusworth, Itziar Irakulis Loitxate, Manuel Montesino San Martin, Bram Maasakkers, Berend Schuit, and Ilse Aben for providing feedback on early drafts of this manuscript.

REFERENCES

- (1) Intergovernmental Panel on Climate Change (IPCC). *Climate Change 2021 The Physical Science Basis*; Cambridge University Press, 2023. https://doi.org/10.1017/9781009157896.
- (2) Saunois, M.; Martinez, A.; Poulter, B.; Zhang, Z.; Raymond, P. A.; Regnier, P.; Canadell, J. G.; Jackson, R. B.; Patra, P. K.; Bousquet, P.; Ciais, P.; Dlugokencky, E. J.; Lan, X.; Allen, G. H.; Bastviken, D.; Beerling, D. J.; Belikov, D. A.; Blake, D. R.; Castaldi, S.; Crippa, M.; Deemer, B. R.; Dennison, F.; Etiope, G.; Gedney, N.; Höglund-Isaksson, L.; Holgerson, M. A.; Hopcroft, P. O.; Hugelius, G.; Ito, A.; Jain, A. K.; Janardanan, R.; Johnson, M. S.; Kleinen, T.; Krummel, P. B.; Lauerwald, R.; Li, T.; Liu, X.; McDonald, K. C.; Melton, J. R.; Mühle, J.; Müller, J.; Murguia-Flores, F.; Niwa, Y.; Noce, S.; Pan, S.; Parker, R. J.; Peng, C.; Ramonet, M.; Riley, W. J.; Rocher-Ros, G.; Rosentreter, J. A.; Sasakawa, M.; Segers, A.; Smith, S. J.; Stanley, E. H.; Thanwerdas, J.; Tian, H.; Tsuruta, A.; Tubiello, F. N.; Weber, T. S.; van der Werf, G. R.; Worthy, D. E. J.; Xi, Y.; Yoshida, Y.; Zhang, W.; Zheng, B.; Zhu, Q.; Zhu, Q.; Zhuang, Q. Global Methane Budget 2000–2020. Earth Syst Sci Data 2025, 17 (5), 1873–1958. https://doi.org/10.5194/essd-17-1873-2025.
- (3) Brandt, A. R.; Heath, G. A.; Cooley, D. Methane Leaks from Natural Gas Systems Follow Extreme Distributions. *Environ Sci Technol* **2016**, *50* (22), 12512–12520.
- (4) Ehret, T.; De Truchis, A.; Mazzolini, M.; Morel, J. M.; D'Aspremont, A.; Lauvaux, T.; Duren, R.; Cusworth, D.; Facciolo, G. Global Tracking and Quantification of Oil and Gas Methane Emissions from Recurrent Sentinel-2 Imagery. *Environ Sci Technol* **2022**, *56* (14), 10517–10529. https://doi.org/10.1021/acs.est.1c08575.
- (5) Lauvaux, T.; Giron, C.; Mazzolini, M.; d'Aspremont, A.; Duren, R.; Cusworth, D.; Shindell, D.; Ciais, P. Global Assessment of Oil and Gas Methane Ultra-Emitters. *Science* (1979) 2022, 375 (6580), 557–561. https://doi.org/10.1126/science.abj4351.
- (6) Sherwin, E. D.; Rutherford, J. S.; Zhang, Z.; Chen, Y.; Wetherley, E. B.; Yakovlev, P. V.; Berman, E. S. F.; Jones, B. B.; Cusworth, D. H.; Thorpe, A. K.; Ayasse, A. K.; Duren, R. M.; Brandt, A. R. US Oil and Gas System Emissions from Nearly One Million Aerial Site Measurements. *Nature* 2024, 627 (8003), 328–334. https://doi.org/10.1038/s41586-024-07117-5.
- (7) Kunkel, W. M.; Carre-Burritt, A. E.; Aivazian, G. S.; Snow, N. C.; Harris, J. T.; Mueller, T. S.; Roos, P. A.; Thorpe, M. J. Extension of Methane Emission Rate Distribution for Permian Basin Oil and Gas Production Infrastructure by Aerial LiDAR. *Environ Sci Technol* **2023**, *57* (33), 12234–12241. https://doi.org/10.1021/acs.est.3c00229.
- (8) Alvarez, R. A.; Zavala-Araiza, D.; Lyon, D. R.; Allen, D. T.; Barkley, Z. R.; Brandt, A. R.; Davis, K. J.; Herndon, S. C.; Jacob, D. J.; Karion, A.; others. Assessment of Methane Emissions from the US Oil and Gas Supply Chain. *Science* (1979) **2018**, 361 (6398), 186–188.
- (9) Allen, D. T.; Torres, V. M.; Thomas, J.; Sullivan, D. W.; Harrison, M.; Hendler, A.; Herndon, S. C.; Kolb, C. E.; Fraser, M. P.; Hill, A. D.; Lamb, B. K.; Miskimins, J.; Sawyer,

- R. F.; Seinfeldi, J. H. Measurements of Methane Emissions at Natural Gas Production Sites in the United States. *Proc Natl Acad Sci U S A* **2013**, *110* (44), 17768–17773. https://doi.org/10.1073/pnas.1304880110.
- (10) Zavala-Araiza, D.; Lyon, D.; Alvarez, R. A.; Palacios, V.; Harriss, R.; Lan, X.; Talbot, R.; Hamburg, S. P. Toward a Functional Definition of Methane Super-Emitters: Application to Natural Gas Production Sites. *Environ Sci Technol* **2015**, *49* (13), 8167–8174. https://doi.org/10.1021/acs.est.5b00133.
- (11) Tyner, D. R.; Johnson, M. R. Where the Methane Is—Insights from Novel Airborne LiDAR Measurements Combined with Ground Survey Data. *Environ Sci Technol* **2021**, *55* (14), 9773–9783.
- (12) Johnson, M. R.; Conrad, B. M.; Tyner, D. R. Creating Measurement-Based Oil and Gas Sector Methane Inventories Using Source-Resolved Aerial Surveys. *Commun Earth Environ* **2023**, *4* (1). https://doi.org/10.1038/s43247-023-00769-7.
- (13) Johnson, M. R.; Conrad, B. M.; Tyner, D. R. Creating Measurement-Based Oil and Gas Sector Methane Inventories Using Source-Resolved Aerial Surveys. *Commun Earth Environ* **2023**, *4* (1). https://doi.org/10.1038/s43247-023-00769-7.
- (14) Donahue, C. P.; Oberoi, K.; Dillon, J. W.; Hengst, V.; Kennedy, B.; Lennox, J.; Rehbein, E.; Sykes, R.; Dudiak, C. D.; Altamura, D. T.; Doherty, G.; Roos, P. A.; Brasseur, J. K.; Thorpe, M. J. Aerial LiDAR-Based, Source-Resolved Methane Emissions Inventory: Permian.
- (15) Cusworth, D. H.; Duren, R. M.; Thorpe, A. K.; Olson-Duvall, W.; Heckler, J.; Chapman, J. W.; Eastwood, M. L.; Helmlinger, M. C.; Green, R. O.; Asner, G. P.; Dennison, P. E.; Miller, C. E. Intermittency of Large Methane Emitters in the Permian Basin. *Environ Sci Technol Lett* **2021**, *8* (7), 567–573. https://doi.org/10.1021/acs.estlett.1c00173.
- (16) Chen, Y.; Sherwin, E. D.; Berman, E. S. F.; Jones, B. B.; Gordon, M. P.; Wetherley, E. B.; Kort, E. A.; Brandt, A. R. Quantifying Regional Methane Emissions in the New Mexico Permian Basin with a Comprehensive Aerial Survey. *Environ Sci Technol* **2022**, *56* (7), 4317–4323. https://doi.org/10.1021/acs.est.1c06458.
- (17) ENVIRONMENTAL PROTECTION AGENCY 40 CFR Part 60 Standards of Performance for New, Reconstructed, and Modified Sources and Emissions Guidelines for Existing Sources: Oil and Natural Gas Sector Climate Review. www.regulations.gov/.
- (18) Vaughan, A.; Mateo-Garcia, G.; Irakulis-Loitxate, I.; Watine, M.; Fernandez-Poblaciones, P.; Turner, R. E.; Requeima, J.; Gorroño, J.; Randles, C.; Caltagirone, M.; Cifarelli, C. AI for Operational Methane Emitter Monitoring from Space. **2024**.
- (19) Varon, D. J.; Jervis, D.; McKeever, J.; Spence, I.; Gains, D.; Jacob, D. J. High-Frequency Monitoring of Anomalous Methane Point Sources with Multispectral Sentinel-2 Satellite Observations. *Atmos Meas Tech* **2021**, *14* (4), 2771–2785. https://doi.org/10.5194/amt-14-2771-2021.

- (20) Jacob, D. J.; Varon, D. J.; Cusworth, D. H.; Dennison, P. E.; Frankenberg, C.; Gautam, R.; Guanter, L.; Kelley, J.; McKeever, J.; Ott, L. E.; Poulter, B.; Qu, Z.; Thorpe, A. K.; Worden, J. R.; Duren, R. M. Quantifying Methane Emissions from the Global Scale down to Point Sources Using Satellite Observations of Atmospheric Methane. *Atmospheric Chemistry and Physics*. Copernicus GmbH July 29, 2022, pp 9617–9646. https://doi.org/10.5194/acp-22-9617-2022.
- (21) Thorpe, A. K.; Green, R. O.; Thompson, D. R.; Brodrick, P. G.; Chapman, J. W.; Elder, C. D.; Irakulis-Loitxate, I.; Cusworth, D. H.; Ayasse, A. K.; Duren, R. M.; Frankenberg, C.; Guanter, L.; Worden, J. R.; Dennison, P. E.; Roberts, D. A.; Chadwick, K. D.; Eastwood, M. L.; Fahlen, J. E.; Miller, C. E. Attribution of Individual Methane and Carbon Dioxide Emission Sources Using EMIT Observations from Space; 2023. https://www.science.org.
- (22) Ramier, A.; Girard, M.; Jervis, D.; Maclean, J.-P.; Marshall, D.; Mckeever, J.; Strupler, M.; Tarrant, E.; Young, D. *High-Resolution Methane Detection with the GHGSat Constellation*; IAF. https://doi.org/10.31223/X5FF0X.
- (23) Jervis, D.; McKeever, J.; Durak, B. O. A.; Sloan, J. J.; Gains, D.; Varon, D. J.; Ramier, A.; Strupler, M.; Tarrant, E. The GHGSat-D Imaging Spectrometer. *Atmos Meas Tech* **2021**, *14* (3), 2127–2140.
- (24) Duren, R.; Cusworth, D.; Ayasse, A.; Howell, K.; Diamond, A.; Scarpelli, T.; Kim, J.; O'neill, K.; Lai-Norling, J.; Thorpe, A.; Zandbergen, S. R.; Shaw, L.; Keremedjiev, M.; Guido, J.; Giuliano, P.; Goldstein, M.; Nallapu, R.; Barentsen, G.; Thompson, D. R.; Roth, K.; Jensen, D.; Eastwood, M.; Reuland, F.; Adams, T.; Brandt, A.; Kort, E. A.; Mason, J.; Green, R. O. The Carbon Mapper Emissions Monitoring System. June 2, 2025. https://doi.org/10.5194/egusphere-2025-2275.
- (25) Pandey, S.; Worden, J.; Cusworth, D. H.; Varon, D. J.; Thill, M. D.; Jacob, D. J.; Bowman, K. W. Relating Multi-Scale Plume Detection and Area Estimates of Methane Emissions: A Theoretical and Empirical Analysis. *Environ Sci Technol* 2025, 59 (16), 7931–7947. https://doi.org/10.1021/acs.est.4c07415.
- (26) Scarpelli, T. R.; Roy, E.; Jacob, D. J.; Sulprizio, M. P.; Tate, R. D.; Cusworth, D. H. Using New Geospatial Data and 2020 Fossil Fuel Methane Emissions for the Global Fuel Exploitation Inventory (GFEI) V3. https://doi.org/10.7910/DVN/HH4EUM.
- (27) Ehret, T.; De Truchis, A.; Mazzolini, M.; Morel, J.-M.; Lauvaux, T.; Duren, R.; Cusworth, D.; Facciolo, G. Global Tracking and Quantification of Oil and Gas Methane Emissions from Recurrent Sentinel-2 Imagery. **2021**.
- (28) Cusworth, D. H.; Thorpe, A. K.; Ayasse, A. K.; Stepp, D.; Heckler, J.; Asner, G. P.; Miller, C. E.; Yadav, V.; Chapman, J. W.; Eastwood, M. L.; Green, R. O.; Hmiel, B.; Lyon, D. R.; Duren, R. M. Strong Methane Point Sources Contribute a Disproportionate Fraction of Total Emissions across Multiple Basins in the United States. 2022. https://doi.org/10.1073/pnas.
- (29) Sherwin, E. D.; Rutherford, J. S.; Chen, Y.; Aminfard, S.; Kort, E. A.; Jackson, R. B.; Brandt, A. R. Single-Blind Validation of Space-Based Point-Source Detection and

- Quantification of Onshore Methane Emissions. *Sci Rep* **2023**, *13* (1). https://doi.org/10.1038/s41598-023-30761-2.
- (30) Sherwin, E. D.; Chen, Y.; Ravikumar, A.; Brandt, A. R. Single-Blind Test of Airplane-Based Hyperspectral Methane Detection via Controlled Releases. **2020**.
- (31) McKeever, J.; Jervis, D. Validation and Metrics for Emissions Detection by Satellite. June 2, 2025. https://doi.org/10.31223/X5DH9Q.
- (32) Mckeever, J.; Jervis, D. *Validation and Metrics for Emissions Detection by Satellite*; 2022. https://www.ghgsat.com/en/case-studies/validation-and-metrics-for-emissions-detection-by-satellite/ (accessed 2024-04-25).
- (33) Ayasse, A. K.; Cusworth, D. H.; Howell, K.; O'Neill, K.; Conrad, B. M.; Johnson, M. R.; Heckler, J.; Asner, G. P.; Duren, R. Probability of Detection and Multi-Sensor Persistence of Methane Emissions from Coincident Airborne and Satellite Observations. *Environ Sci Technol* **2024**. https://doi.org/10.1021/acs.est.4c06702.
- (34) Thorpe, A. K.; Frankenberg, C.; Aubrey, A. D.; Roberts, D. A.; Nottrott, A. A.; Rahn, T. A.; Sauer, J. A.; Dubey, M. K.; Costigan, K. R.; Arata, C.; Steffke, A. M.; Hills, S.; Haselwimmer, C.; Charlesworth, D.; Funk, C. C.; Green, R. O.; Lundeen, S. R.; Boardman, J. W.; Eastwood, M. L.; Sarture, C. M.; Nolte, S. H.; Mccubbin, I. B.; Thompson, D. R.; McFadden, J. P. Mapping Methane Concentrations from a Controlled Release Experiment Using the next Generation Airborne Visible/Infrared Imaging Spectrometer (AVIRIS-NG). *Remote Sens Environ* **2016**, *179*, 104–115. https://doi.org/10.1016/j.rse.2016.03.032.
- (35) Cusworth, D. H.; Bon, D. M.; Varon, D. J.; Ayasse, A. K.; Asner, G. P.; Heckler, J.; Sherwin, E. D.; Biraud, S. C.; Duren, R. M. Duration of Super-Emitting Oil & Gas Methane Sources 1 2.
- (36) Bell, C.; Rutherford, J.; Brandt, A.; Sherwin, E.; Vaughn, T.; Zimmerle, D. Single-Blind Determination of Methane Detection Limits and Quantification Accuracy Using Aircraft-Based LiDAR. *Elementa: Science of the Anthropocene* **2022**, *10* (1). https://doi.org/10.1525/elementa.2022.00080.
- (37) McLinden, C. A.; Griffin, D.; Davis, Z.; Hempel, C.; Smith, J.; Sioris, C.; Nassar, R.; Moeini, O.; Legault-Ouellet, E.; Malo, A. An Independent Evaluation of GHGSat Methane Emissions: Performance Assessment. *Journal of Geophysical Research: Atmospheres* **2024**, *129* (15). https://doi.org/10.1029/2023JD039906.
- (38) Biener, K. J.; Gorchov Negron, A. M.; Kort, E. A.; Ayasse, A. K.; Chen, Y.; MacLean, J. P.; McKeever, J. Temporal Variation and Persistence of Methane Emissions from Shallow Water Oil and Gas Production in the Gulf of Mexico. *Environ Sci Technol* **2024**, *58* (11), 4948–4956. https://doi.org/10.1021/acs.est.3c08066.
- (39) Jervis, D.; Girard, M.; MacLean, J.-P. W.; Marshall, D.; McKeever, J.; Strupler, M.; Ramier, A.; Tarrant, E.; Young, D.; Maasakkers, J. D.; Aben, I.; Scarpelli, T. R. Global Energy Sector Methane Emissions Estimated by Using Facility-Level Satellite Observations.

- (40) Varon, D. J.; Jacob, D. J.; McKeever, J.; Jervis, D.; Durak, B. O. A.; Xia, Y.; Huang, Y. Quantifying Methane Point Sources from Fine-Scale Satellite Observations of Atmospheric Methane Plumes. *Atmos Meas Tech* **2018**, *11* (10), 5673–5686.
- (41) Duren, R. M.; Thorpe, A. K.; Foster, K. T.; Rafiq, T.; Hopkins, F. M.; Yadav, V.; Bue, B. D.; Thompson, D. R.; Conley, S.; Colombi, N. K.; others. California's Methane Super-Emitters. *Nature* **2019**, *575* (7781), 180–184.
- (42) Thompson, D. R.; Leifer, I.; Bovensmann, H.; Eastwood, M.; Fladeland, M.; Frankenberg, C.; Gerilowski, K.; Green, R. O.; Kratwurst, S.; Krings, T.; Luna, B.; Thorpe, A. K. Real-Time Remote Detection and Measurement for Airborne Imaging Spectroscopy: A Case Study with Methane. *Atmos Meas Tech* **2015**, 8 (10), 4383–4397. https://doi.org/10.5194/amt-8-4383-2015.
- (43) Vaughan, A.; Mateo-García, G.; Gómez-Chova, L.; Ruzička, V.; Guanter, L.; Irakulis-Loitxate, I. CH4Net: A Deep Learning Model for Monitoring Methane Super-Emitters with Sentinel-2 Imagery. *Atmos Meas Tech* **2024**, *17* (9), 2583–2593. https://doi.org/10.5194/amt-17-2583-2024.
- (44) Rouet-Leduc, B.; Hulbert, C. Automatic Detection of Methane Emissions in Multispectral Satellite Imagery Using a Vision Transformer. *Nat Commun* **2024**, *15* (1). https://doi.org/10.1038/s41467-024-47754-y.
- (45) He, T.-L.; Boyd, R. J.; Varon ID, D. J.; Turner, A. J. Increased Methane Emissions from Oil and Gas Following the Soviet Union's Collapse. **2024**. https://doi.org/10.1073/pnas.

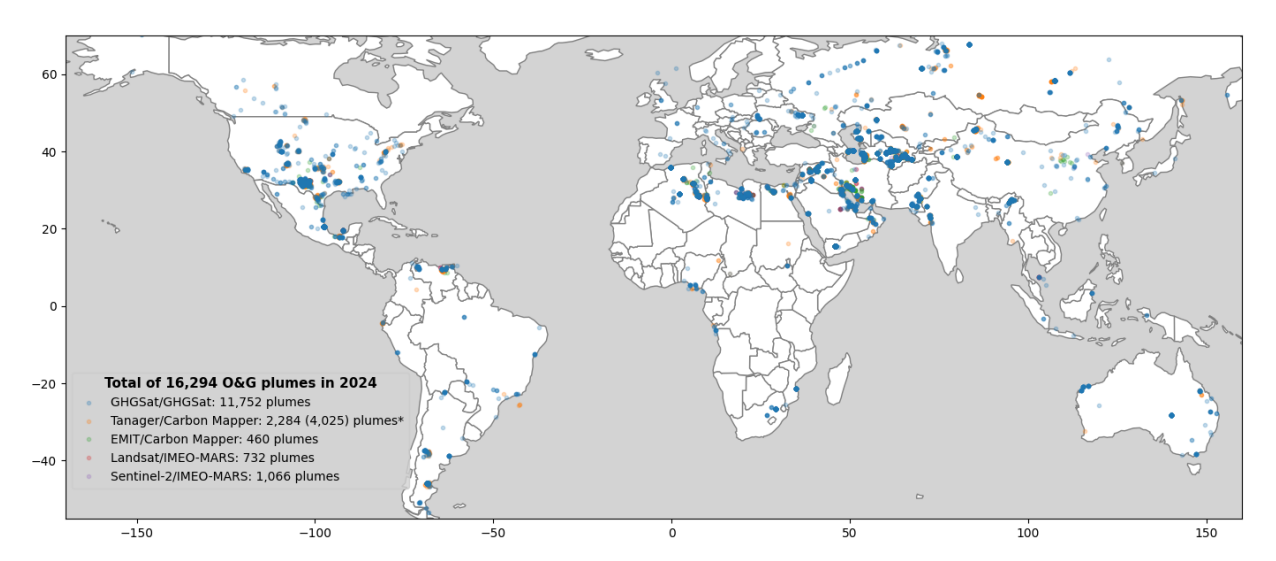
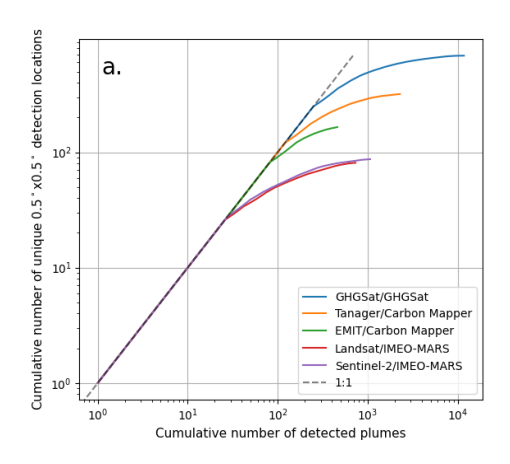


Figure 1: Map of methane plumes detected from oil-gas sources in 2024*. The total number of plumes detected by each satellite is annotated in the legend. *For Tanager/Carbon Mapper, we take plume detections from Sept 19th, 2024 (immediately after launch) until August 31st, 2025. The number of plumes in parentheses is our estimate of the total annual O&G emissions Tanager/Carbon Mapper would have detected in a full calendar year.



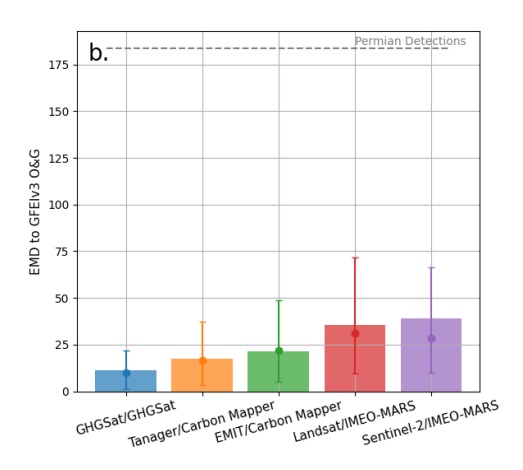


Figure 2: Spatial distribution of detected plumes. a) The number of unique locations 0.5° x 0.5° where a plume detection was found versus the ranked number of plume detections. b) The Earth Movers Distance (in dimensionless units) calculated between gridded plume detection locations and the GFEIv3 O&G inventory. The plume detection locations are gridded to 0.5° x 0.5° resolution and the unit of the EMD is distance (in grid cell units) to move a unit of detection location probability onto the GFEIv3 emissions probability distribution. The bar data indicates the EMD between detected plume detection locations for each satellite system and GFEIv3. The marker and error bars indicate the mean and (10%, 90%) values of M_k random, emission-weighed and non-repeated samples of GFEIv3, where $M_k \leq N_k$ is the number of unique gridded detection locations for each satellite system. The EMD between GFEIv3 and grid cells that had a detection by any satellite system in the Permian basin region is calculated for reference and shown as a dashed line.

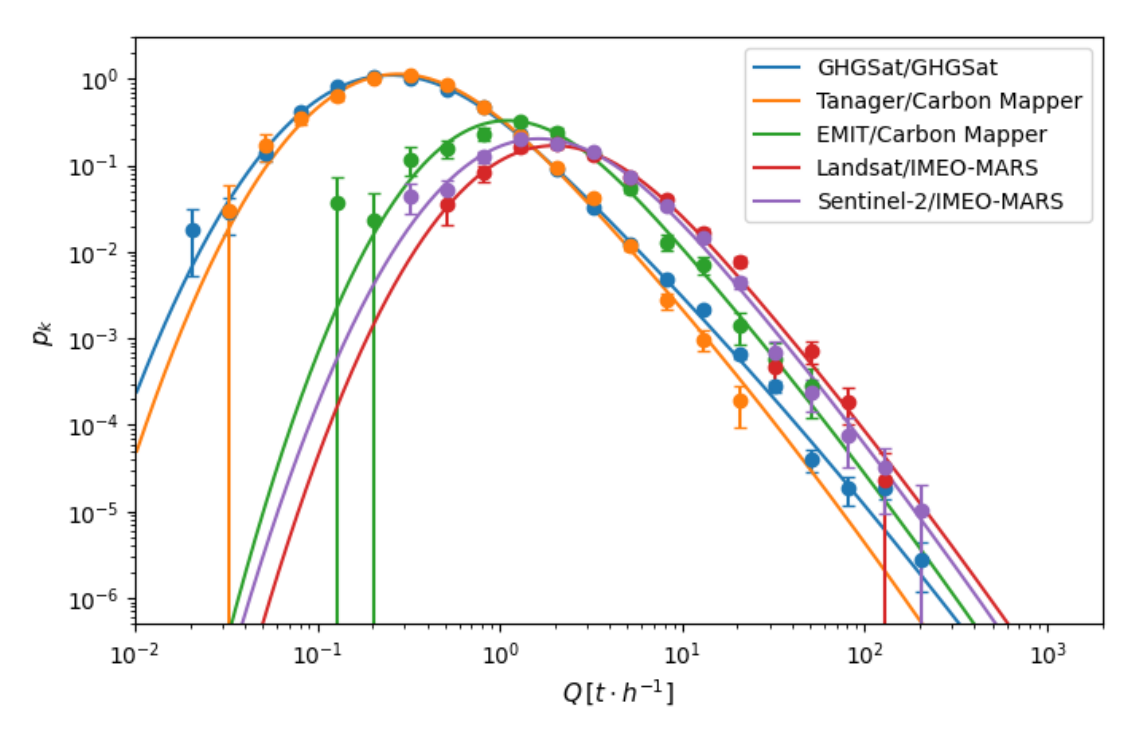


Figure 3: Measured emission rate density distributions $p_{k;i}$ for the six different satellite systems studied. Measured data points with error bars provided for visualization (estimated from counting statistics as $p_{k;i} \cdot n_{k;i}^{-0.5}$). The lines are the retrieved models $\hat{p}_{k;i}(\hat{z}_k, \hat{\theta}_k)$.

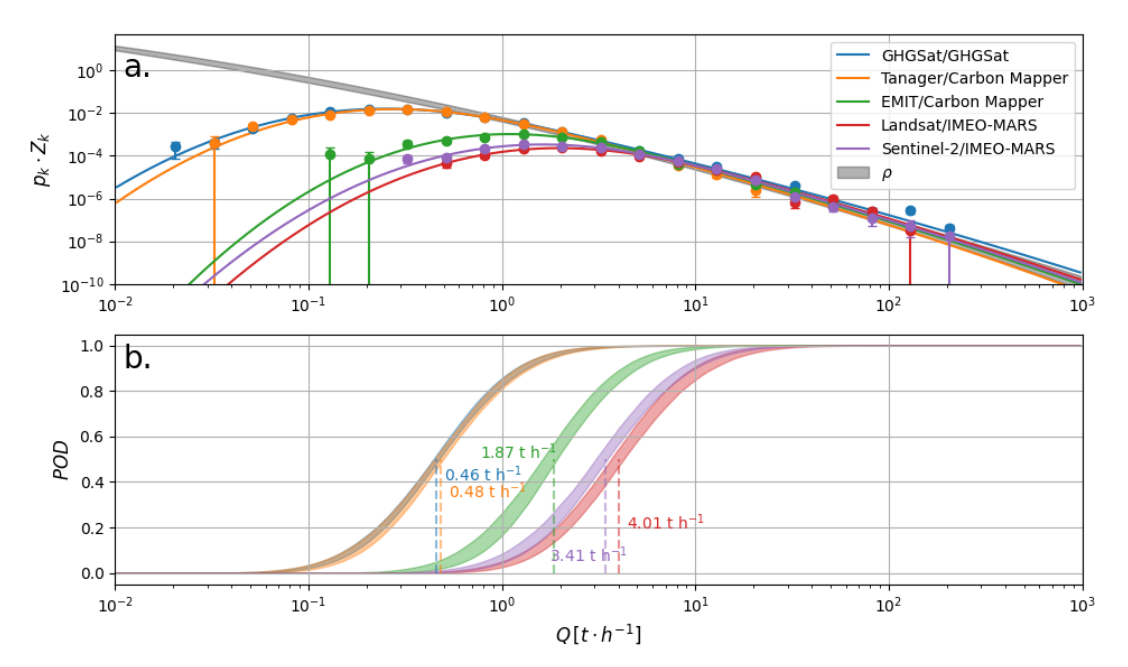


Figure 4: Scaled measured emission rate density distributions and estimated detection probability. a) The measured emission rate density $p_{k;i}$ scaled by the detection fraction Z_k , as well as the estimated emission rate density distribution $\rho(Q; \langle \widehat{\theta} \rangle)$. b) The estimated survey-mode detection probability $POD_k(Q; \widehat{\mathbf{z}}_k)$ with (10%, 90%) confidence bounds. The emission rates corresponding to a 50% probability of detection are annotated for each instrument and illustrated with a dashed vertical line.

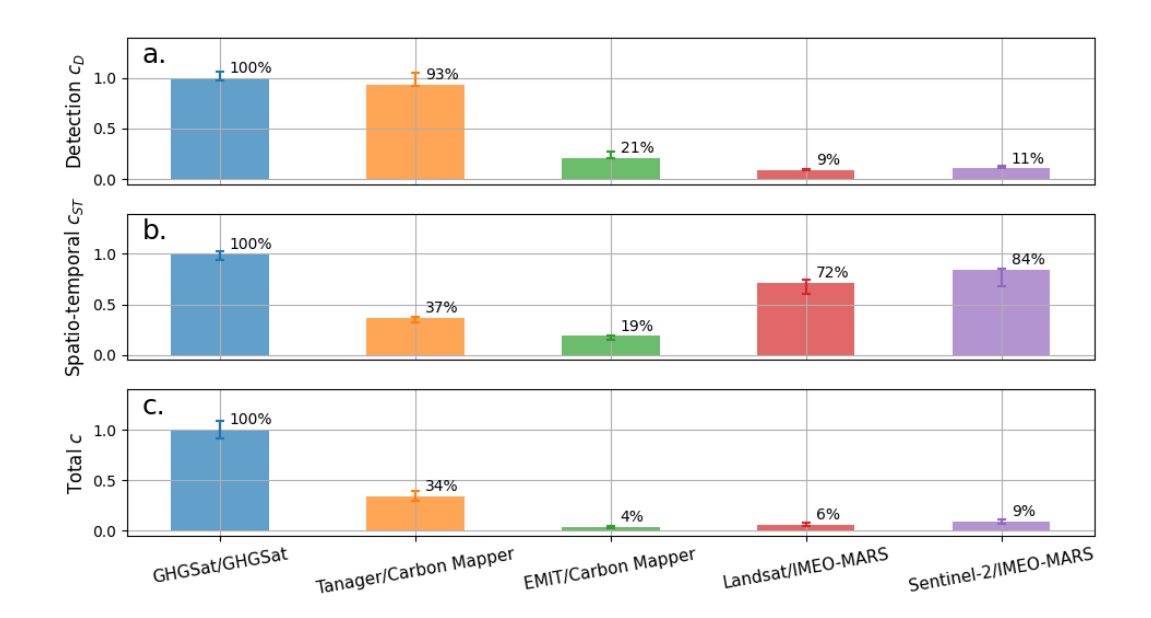


Figure 5: Relative completeness measures for satellite/data provider systems. a) The relative detection completeness c_D . b) The relative spatio-temporal completeness c_{ST} . c) The relative total completeness c. Error bars encompass the (10%, 90%) percentile estimates of the bootstrap results.

SUPPORTING INFORMATION: Estimating the Global Oil-Gas Methane Emission Rate Distribution at Facility Scale using Multiple Satellite Systems

Dylan Jervis¹(dylan.jervis@ghgsat.com), Jean-Philippe W MacLean¹, Jason McKeever¹, Mathias Strupler¹, Antoine Ramier¹

¹GHGSat Inc, Montreal, QC, Canada

Summary: 15 pages, 5 figures, 2 tables

TABLE OF CONTENTS S1 Satellite Instruments and Data providers	24
S2 Akaike Information Criteria for determining best fit functions	26
S3 Earth Movers Distance	28
S4 Estimating Tanager/Carbon Mapper Annual O&G Plume Count	31
S5 Joint and Satellite System Specific POD and PDF estimates	32
S6 Spatial Resolution Dependence of Measured Emission Rate Distributions	33

S1 Satellite Instruments and Data providers

GHGSat: The GHGSat methane satellite constellation comprises 12 commercial satellites as of October 2025 (though only data from 10 methane satellites were in operation in 2024 and therefore used in this 2024 study), all of whom travel in a sun-synchronous orbit at approximately 500 km altitude. The instruments capture solar backscattered radiation between the wavelengths of 1630 - 1670 nm and the light is spectrally filtered using a wide-angle Fabry-Perot spectrometer(I). The methane column density is retrieved with a ~25 m ground sample distance over targeted 15 x 12 – 15 x 30 km² retrieval domains.

Candidate methane enhancement plumes in the column density fields are first identified with a machine learning model. Human operation technicians then inspect each candidate plume enhancement to either validate or reject the plume. For validated plumes, the plume enhancement is delineated from the background using a semi-automated floodfill algorithm. Once the plume has been masked, the source rate is estimated using an IME method(2) using wind speed from a 3rd-party meteorological reanalysis product (OpenWeather) at the location and time of observation. The origin of the plume is estimated by the human operator and attributed to a sector based on facility type identification.

Tanager: Carbon Mapper is a non-profit organization based in Pasadena, California that leads a public-private coalition including Planet Labs, NASA-JPL, the State of California, the University of Arizona, the Rocky Mountain Institute, and others. The Tanager satellite, Tanager-1, from Carbon Mapper was launched on August 16, 2024 and started delivering methane plumes on September 19th, 2024. The instrument is a push-broom grating instrument spanning the 400 − 2,500 nm spectral region with ~5.5 nm spectral sampling(3) and a 500 km, sun-synchronous orbit(4). The mean sample distance is calculated to be 38m from their observation specific data between September 19th, 2024 and May 7th, 2025. The standard sensitivity mode results in retrieval domains that are 19 km x 481 km in area. Plumes are identified, then segmented with an automated procedure that identifies connected and nearly-connected plume enhancements. The emission rate is estimated using the IME method described in Ref(5). The Tanager methane emission rate data is obtained from the Carbon Mapper data portal (https://data.carbonmapper.org/).

EMIT: The NASA/JPL Earth Surface Mineral Dust Source Investigation (EMIT) has been mounted on the International Space Station (ISS) since 2022, orbiting at an altitude of approximately 400 km. EMIT is an imaging spectrometer able to collect contiguous spectra between 380 - 2,500 nm with \sim 7.4 nm spectral resolution(3). The ground sample distance is approximately 60 m and the push-broom array collects spectra from \sim 80 km-wide swaths in dust emitting regions(6). The methane column density enhancement is estimated using a matched filter technique(6, 7). Methane enhancements corresponding to

plumes are identified and delineated using a semi-automated procedure that collects plume enhancements within a 200m "merge" distance, and up to a 1000m maximum "fetch" distance. The emission rate is estimated using an IME method with wind speed provided by ECMF ERA5 hourly data(6). EMIT methane emission rate data was obtained from the Carbon Mapper data portal (https://data.carbonmapper.org/).

Sentinel-2: The Sentinel-2 mission consists of polar-orbiting satellites (Sentinel-2A launched in 2015, Sentinel-2B launched in 2017, Sentinel-2C launched in September 2024) at an altitude of approximately 800 km altitude, with an equator crossing time of approximately 10:30 (local solar time) and a cross-track swath of 290km(8), providing a ~5-day revisit time at the equator. The Sentinel-2 mission is a multispectral instrument, with the methane sensitive band, Band 12, having a spectral width of approximately 90nm with a ground sample distance of 20m. Methane column density enhancements can be estimated using band reflectance ratios (8) and/or machine learning methods(9–11). Sentinel-2 methane emissions data is provided via the IMEO-MARS Eye on Methane data platform (https://methanedata.unep.org/).

Landsat: Landsat 8 was launched in 2013 and Landsat 9 was launched in 2021, both orbiting in a sunsynchronous 705 km altitude orbit with a combined ~8-day revisit time. The instrument collects backscattered radiation between 430 – 2,300 nm, with the methane sensitive Band 7 having a ~200 nm bandwidth. The Landsat multispectral instruments have demonstrated the ability to detect methane plumes(12, 13) using similar techniques employed for the Sentinel-2 instruments(8, 11). Landsat methane emissions data is obtained from the IMEO-MARS Eye on Methane data platform (https://methanedata.unep.org/).

S2 Akaike Information Criteria for determining best fit functions

The Akaike Information Criteria (AIC) is a statistical measure of a model's predictive quality and is given by:

$$AIC(l, \mathbf{z}, \boldsymbol{\theta}) = 2l - 2\log \mathcal{L}(\mathbf{z}, \boldsymbol{\theta} | \boldsymbol{Q})$$
(1)

where l is equal to the number of parameters in the model and $\mathcal{L}(\mathbf{z}, \boldsymbol{\theta} | \boldsymbol{Q})$ is the likelihood. A lower AIC indicates a more predictive model since it suggests a better combination of fitting the data well (lower NLL) and fewer parameters (thus preventing overfitting).

We first use the AIC to estimate the relative prediction quality of a lognormal probability distribution function versus a power law model for the emission rate distribution $\rho(\theta)$. The lognormal model is defined in equation 3 of the main text and repeated here:

$$\rho_{log}(Q;\boldsymbol{\theta}_{log}) = \frac{1}{Q\sigma_{\nu}\sqrt{2\pi}}e^{-\frac{(\ln(Q)-\mu)^2}{2\sigma}}$$
(2)

And the power law model is defined as

$$\rho_{power}(Q; \boldsymbol{\theta}_{power}) = bQ^{-\alpha} \tag{3}$$

Where $b = \frac{1-\alpha}{Q_{max}^{1-\alpha} - Q_{min}^{1-\alpha}}$ ($\alpha \neq 1$, with the $\alpha = 1$ case using the logarithmic normalization) is a

normalization constant defined from the emission rate bounds $\{Q_{min}, Q_{max}\}$ corresponding to the minimum and maximum emission rate bin edges. As in the first stage of our estimation procedure, we assume a common emission rate distribution across all satellite systems while allowing satellite system specific detection probability parameters. Thus, the number of parameters for the lognormal and power law models are $l_{joint-log} = 2K + 2$ and $l_{joint-pow} = 2K + 1$, respectively, for K = 5 satellite systems (two POD parameters per satellite plus $\{\mu, \sigma\}$ or $\{\alpha\}$ for ρ). We find an AIC difference of

$$\Delta AIC = AIC_{joint-log} - AIC_{joint-pow} = -1.14 \tag{4}$$

That is, the lognormal has the lower AIC by 1.14 points which can be interpreted as the lognormal model being approximately $e^{\Delta AIC/2} \approx 2$ times as probable as the power law at minimizing the information loss. Figure S1 shows a comparison of the joint lognormal and power law fits to the data. We find a best-fit power-law exponent of $\hat{\alpha} = 2.29$.

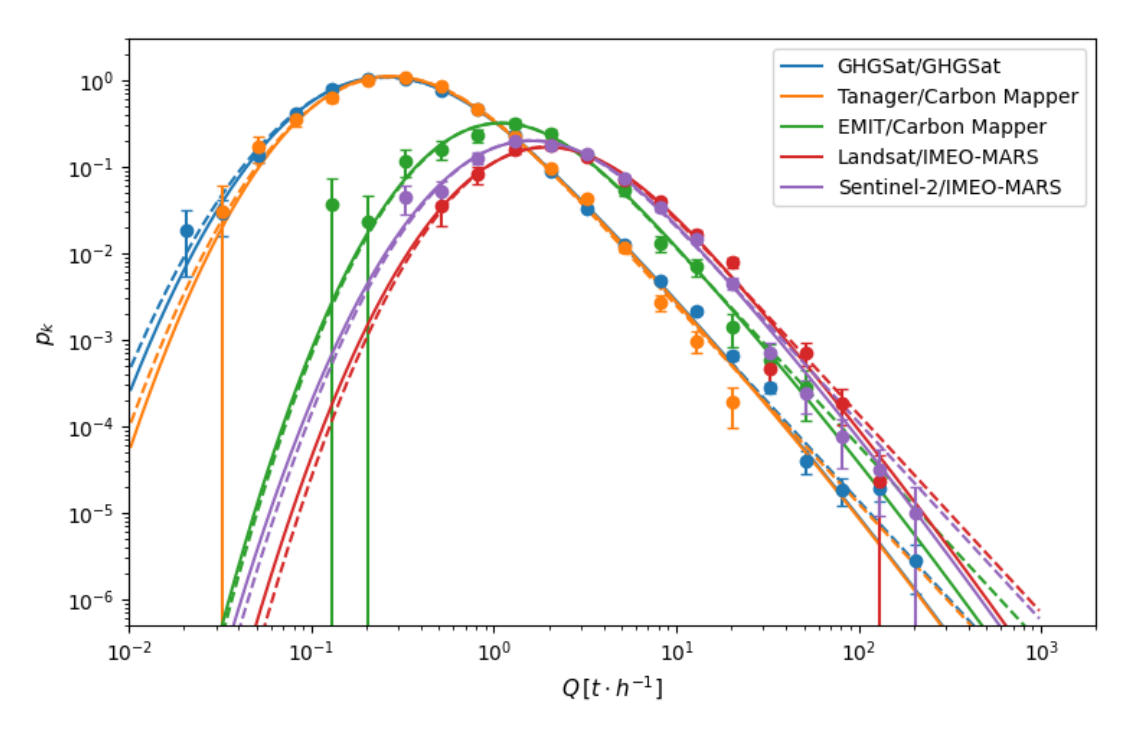


Figure S1: Empirical and modelled emission rate distributions. Solid lines correspond to the lognormal model, dashed lines to the power law model. Both lognormal and power law emission rate distribution models are common to all satellite systems in the fit.

Having established that a lognormal emission rate distribution model is preferred, we then examined whether the emission rate distribution model should be common across satellite systems or satellite system specific. For the joint (common) model, we fit $l_{joint-log} = 2K + 2$ parameters $\{\hat{\boldsymbol{z}}_{joint;k}, \hat{\boldsymbol{\theta}}_{joint}\}$; and for the independent model we fit $l_{ind-log} = (2+2)K$ parameters $\{\hat{\boldsymbol{z}}_k, \hat{\boldsymbol{\theta}}_k\}$. Comparing the AIC difference evaluated on the same data, we find

$$\Delta AIC = AIC_{joint-log} - \sum_{k=1}^{K} AIC_{ind-log;k} = 18.9,$$
 (5)

meaning that the satellite system specific model has the lower (better) AIC by 18.9 points, indicating that the satellite specific emission rate assumption is $e^{18.9/2} \approx 13,000$ times as probable as the common emission rate model at minimizing the information loss. We therefore report parameter estimation results from our second stage (Bayesian penalized independent) fits, which retain this improved predictive quality while stabilizing weakly identified parameters.

S3 Earth Movers Distance

The Earth Movers Distance (EMD) estimates the minimum work required to transform one distribution into another. We use the python function 'ot.emd2(a, b, M)' to calculate the two-dimensional EMD between distributions $\mathbf{A} = (a_i, x_i)^n_{i=1}$ and $\mathbf{B} = (b_j, y_j)^m_{j=1}$ with weight vectors $\mathbf{a} = (a_i)^n_{i=1}$ and $\mathbf{b} = (a_i)^n_{i=1}$ and the distance metric between latitude/longitude $\mathbf{x} = (\phi, \lambda)$ points given by \mathbf{M} . The distributions are normalized such that $1 = \sum_i^n a_i = \sum_j^m b_j$. The problem is to find the transport flow matrix $F_{i,j}$ that minimizes the work function

$$W(F) = \sum_{i,j} F_{i,j} d_{i,j} \tag{6}$$

where we choose $d_{i,j} = |x_i - y_j|$ to be the Euclidean distance, and $F_{i,j}$ is subject to the marginal constraints $\sum_{i=1}^{n} F_{i,j} = b_j$ and $\sum_{i=1}^{m} F_{i,j} = a_i$.

We choose to calculate the EMD between each satellite's detection locations – gridded to 0.5 deg x 0.5 deg spatial resolution for speed – and the Global Fuel Exploitation Inventory version 3 (GFEIv3)(14). Specifically, we use the sum of the "Oil_All" and "Gas_All" GFEIv3 fields. For the satellite system detections, we assign a uniform weight in a given grid cell if a satellite has observed at least one plume there. We use the GFEIv3 estimated emission flux in each grid cell to weight the GFEIv3 probability distribution, under the assumption that detections are more representative of GFEIv3 predicted emissions if they occur near locations where GFEIv3 predicts larger emission fluxes. The GFEIv3 Oil and Gas flux is shown in Figure S2.

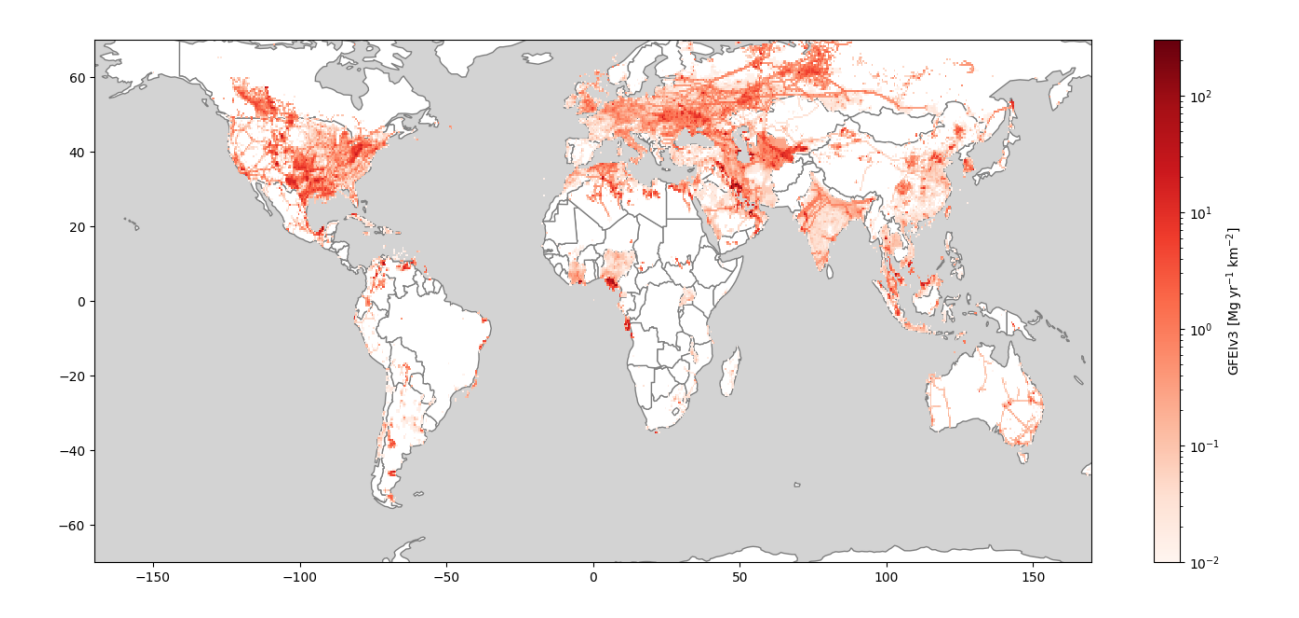


Figure S2: The GFEIv3 Oil and Gas flux used in the Earth Mover's Distance calculation.

As a point of reference, we also calculate the EMD between M_k samples of GFEIv3 O&G and the full GFEIv3 O&G distribution, where $M_k \leq N_k$ are the unique grid cells that contain a detection for satellite system k, tabulated in Table S1. The M_k samples are weighted by the GFEIv3 emissions in each grid cell (calculated by multiplying the GFEIv3 flux by the area of each grid cell). We do this 100 times for each satellite system, generating 100 different M_k samples of GFEIv3. We calculate the mean and (10%, 90%) percentile and compare to the EMD calculate for the measured plume detection locations. The fact that all satellite system measured EMDs are within the (10%, 90%) percentile sampled EMD values, suggests that the satellite systems have representative spatial coverage of inventory-predicted O&G emission locations.

Satellite System	Number of plumes N_k	Unique 0.5° x 0.5° grid cells with at least one detection M_k
GHGSat/GHGSat	11,752	687
Tanager/Carbon Mapper	2,284	319
EMIT/Carbon Mapper	460	165
Sentine-2/IMEO-MARS	1,066	87
Landsat/IMEO-MARS	732	81

Table S1: Number of detected plumes and unique grid cells where detections occurred.

S4 Estimating Tanager/Carbon Mapper Annual O&G Plume Count

The Tanager/Carbon Mapper dataset is the only one of the 5 satellite systems for which we do not have a full year's worth of emissions in 2024, owing to its launch on August 19th, 2024. To estimate the number of plumes it would have detected in a full years-worth of nominal operations, we take the average of the plume count per day (from Tanager CH4 O&G plume data pulled from the Carbon Mapper data portal on July 14th, 2025) between February 2nd, 2025 and July 13th, 2025 (see Figure S3). This is a period that starts after Tanager reached nominal operational capacity. We estimate that an average rate of 11.03 O&G plumes are detected per day from Tanager/Carbon Mapper and, consequently, 4,025 O&G plumes per year.

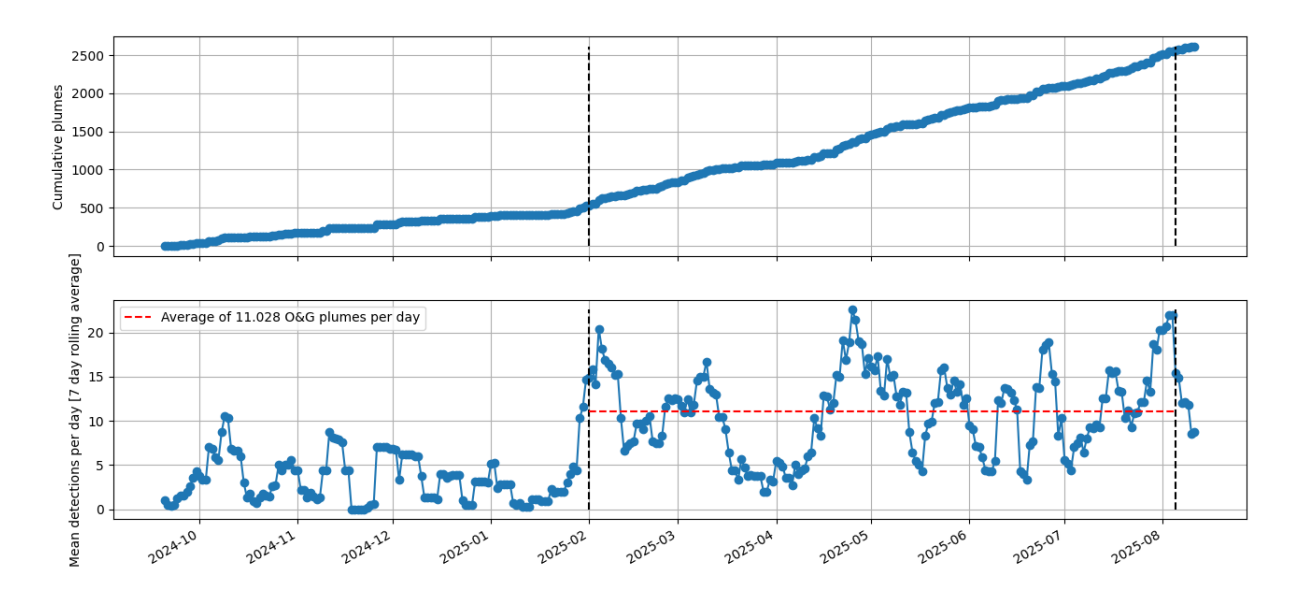


Figure S3: Tanager/Carbon Mapper O&G CH4 plume detections. The top plot shows the cumulative number of O&G plumes detected since launch. The bottom plot shows the 7-day rolling average of the mean plumes detected per day. The dashed vertical lines show the time period over which nominal average plumes per day estimate was calculated (red horizontal dashed line).

S5 Joint and Satellite System Specific POD and PDF estimates

For the first stage results, where a common lognormal emission rate distribution is assumed, we retrieve the following for the mean and bootstrap estimates for the emission rate distribution parameters:

$$\left(\hat{\mu}_{joint} \pm \delta\hat{\mu}_{joint}, \hat{\sigma}_{joint} \pm \widehat{\delta\sigma}_{joint}\right) = (-6.73 \pm 1.72, 2.61 \pm 0.25)$$

The satellite system specific parameters for both the first (joint) and second stage (independent with penalty) results are shown in Table S2 alongside the bootstrap standard errors used to regularize the penalty terms.

Instrument	$\widehat{Q}_{joint;det}$	\hat{s}_{joint}	$\delta(\log \widehat{Q}_{joint;det})$	$\delta(\log \hat{s}_{joint})$	\widehat{Q}_k	\hat{s}_k	$\hat{\mu}_k$	$\hat{\sigma}_k$
GHGSat/GHGSat	0.48	0.78	0.09	0.023	0.46	0.77	-7.44	2.78
Tanager/Carbon Mapper	0.44	0.72	0.08	0.025	0.48	0.73	-6.03	2.36
EMIT/Carbon Mapper	1.79	0.67	0.09	0.050	1.87	0.66	-6.87	2.53
Landsat/IMEO- MARS	3.96	0.72	0.09	0.038	4.01	0.72	-6.67	2.57
Sentinel-2/IMEO- MARS	3.29	0.73	0.07	0.034	3.41	0.73	-6.62	2.53

Table S2: Retrieved POD and PDF parameters.

S6 Spatial Resolution Dependence of Measured Emission Rate Distributions

When an instrument's spatial resolution is coarse relative to individual sources, what it detects is the sum of multiple equipment-level plumes within its facility-scale resolution. Suppose J pieces of equipment are emitting at rates Q_1, \ldots, Q_J with independent source-level distributions $\rho_j(Q; \boldsymbol{\beta}_j)$. The facility-scale emission rate is

$$Q_{fac} = \sum_{j=1}^{J} Q_j \tag{7}$$

And the corresponding facility-scale emission rate distribution is the convolution of the equipment level distributions

$$\rho_{fac}(Q; \boldsymbol{\beta}_{fac}) = (\rho_1 * \rho_2 * \dots * \rho_I)(Q)$$
(8)

Where * denotes convolution. We note that Reference (15) explored the spatial resolution dependence of emission rate distributions in a numerical experiment with a Gamma distribution and the assumption that J grew proportionally to the spatial resolution of the instrument. We validate this analytical model with our own numerical experiment where we assume that we are aggregating I equipment-level sources that are emitting independently with identical power-law emission rate distributions $\rho_i = \rho_{power}(Q; \theta_{power})$ with $(\alpha = 2, \{Q_{min}, Q_{max}\} = \{10^{-4}t \ h^{-1}, 10^{1.5}t \ h^{-1}\})$. We compare the analytical model $\rho_{fac}(Q; \boldsymbol{\beta}_{fac})$ with numerical simulations where 2E6 facility samples are drawn with either I = 1, 10, or 100 aggregated equipment sources that are summed for each facility. In Figure S4, we plot the "true" facility distribution for each case, as well as the "measured" detected facility distribution (with an instrument with 50% POD value at 50 kg h⁻¹). We can see that aggregation introduces a peak in the true distribution that moves to increasingly higher emission rates as I increase (roughly proportionally to I). The large emission rate tails of this true facility distribution are unaffected, however. We can see that the measured emission rate distributions are unaffected as long as the partial detection region lies above this aggregation peak. This is true, in our numerical experiment, for the J = 1 (no aggregation) and J=10 cases, but not for the J = 100case, where an estimate of the POD would be biased high if a I = 1 true emission rate distribution was assumed.

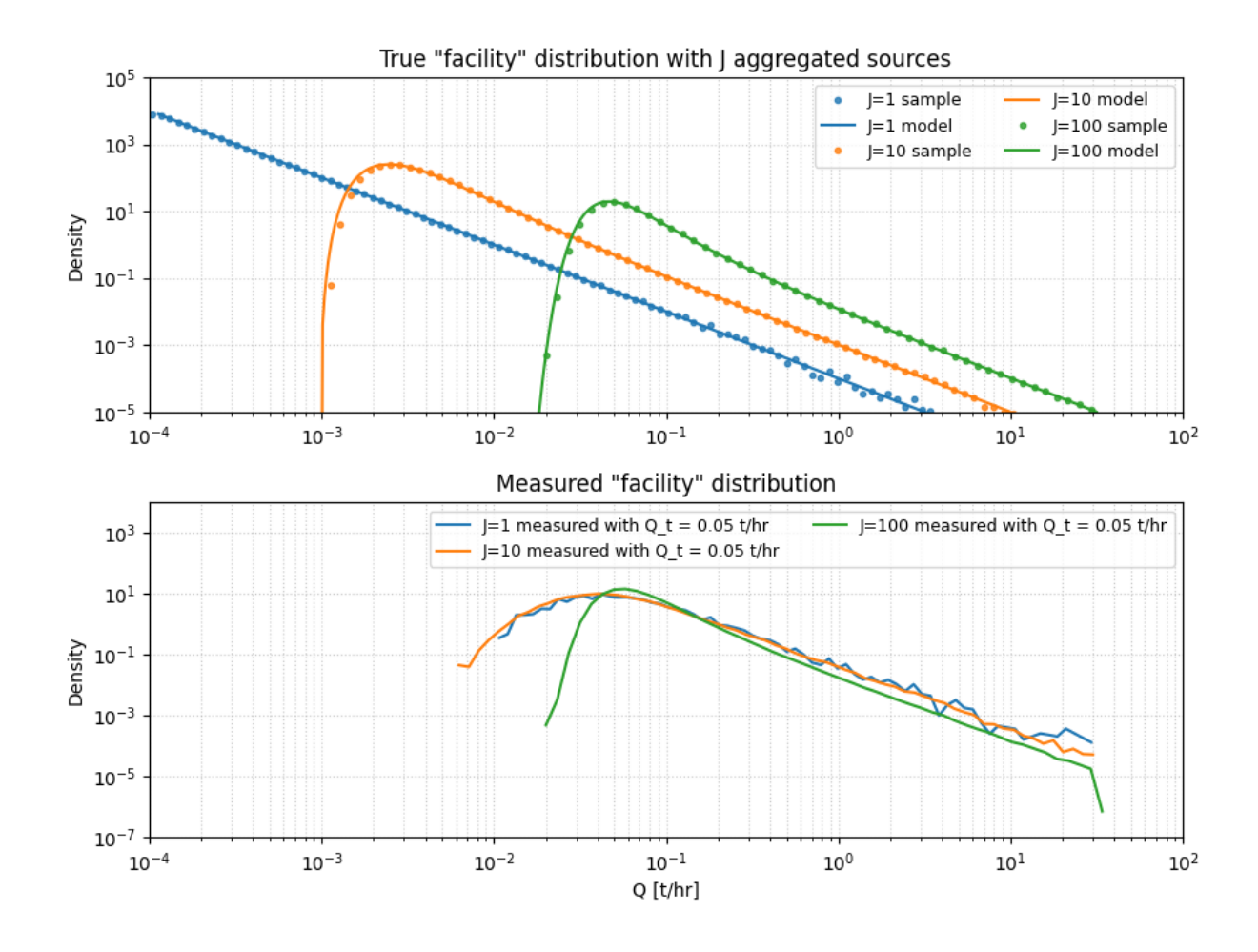


Figure S4: Simulated "true" (top) and "measured" (bottom) facility distributions with *J* aggregated sources.

In our numerical experiment we showed that if the equipment-scale distributions $\rho_j(Q; \beta_j)$ are all heavy-tailed (e.g. lognormal, power-law, etc.), then the facility-scale distribution will be also heavy-tailed with large emission rate tail behaviour driven by the most heavy-tailed of the equipment-scale distributions. Heuristically, this can be understood as the facility-scale distributions being dominated by single, large, equipment-scale emissions. This suggests that even instruments with very different spatial resolutions may retrieve the same tail behaviour. We show this empirically in Figure S5 by performing our two-stage fit of high-resolution satellite detections in the Permian basin alongside i) the 2 m equipment-level measured emission rates from an airborne Bridger GML Permian survey (16) and ii) the \sim 7 km resolution measured emission rates measured by TROPOMI in the Permian basin in 2024. The TROPOMI data is provided to IMEO-MARS through CAMS

(https://apps.atmosphere.copernicus.eu/methane-explore), though the full 2024 data (not all of which is

available on CAMS) was provided directly by SRON. After retrieving each system's detection probability and calculating the detection fraction $Z_k = \int_0^\infty POD(Q)\rho(Q)dQ$, we find that the scaled distributions $Z_k \cdot \hat{p}_k$ share a similarly shaped tail for emission rates where $POD \to 1$, as expected. We note that for TROPOMI, as for the other satellite systems, our model assumes negligible plume aggregation within detected emissions at, or above, the TROPOMI partial detection region.

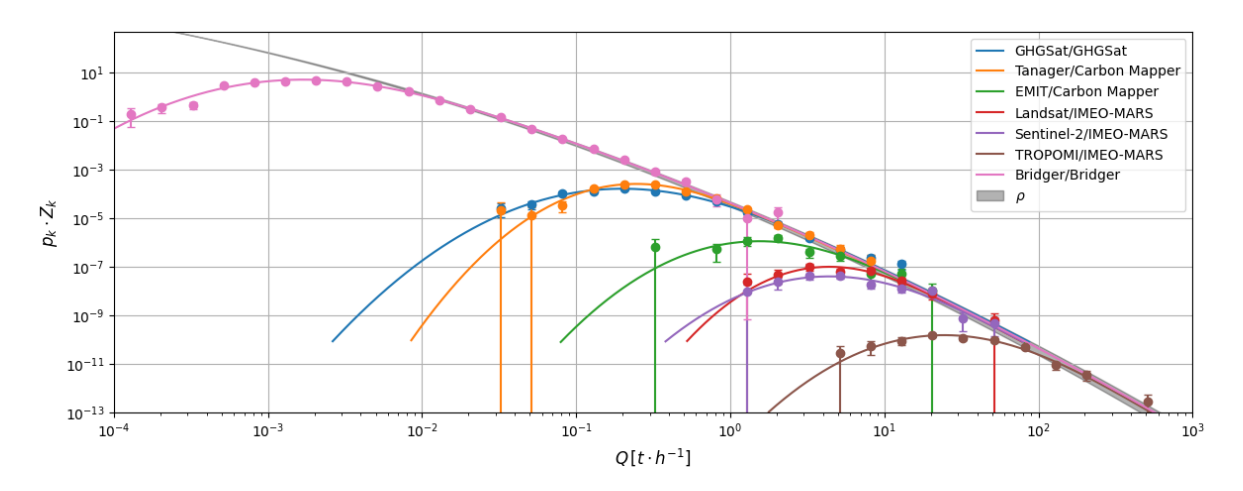


Figure S5: Scaled emission rate distributions measured in the Permian Basin from high resolution satellites (GHGSat/GHGSat, Tanager/Carbon Mapper, EMIT/Carbon Mapper, Landsat/IMEO-MARS, and Sentinel-2/IMEO-MARS), 2 m equipment level airborne measurements (Bridger GML), and 7 km regional level satellite (TROPOMI).